JACS
JOURNAL OF THE AMERICAN CHEMICAL SOCIETY
pubs.acs.org/JACS
Article

Superionic Conducting Halide Frameworks Enabled by Interface-Bonded Halides

Jiamin Fu,[○] Shuo Wang,[○] Jianwen Liang,[○] Sandamini H. Alahakoon, Duojie Wu, Jing Luo, Hui Duan, Shumin Zhang, Feipeng Zhao, Weihan Li, Minsi Li, Xiaoge Hao, Xiaona Li, Jiatang Chen, Ning Chen, Graham King, Lo-Yueh Chang, Ruying Li, Yining Huang, Meng Gu, Tsun-Kong Sham,* Yifei Mo,* and Xueliang Sun*

Cite This: *J. Am. Chem. Soc.* 2023, 145, 2183−2194

Read Online

ACCESS | Metrics & More | Article Recommendations | Supporting Information

ABSTRACT: The revival of ternary halides Li−M−X (M = Y, In, Zr, etc.; X = F, Cl, Br) as solid-state electrolytes (SSEs) shows promise in realizing practical solid-state batteries due to their direct compatibility toward high-voltage cathodes and favorable room-temperature ionic conductivities. Most of the reported superionic halide SSEs have a structural pattern of $[MCl_6]^{x-}$ octahedra and generate a tetrahedron-assisted Li^+ ion diffusion pathway. Here, we report a new class of zeolite-like halide frameworks, $SmCl_3$, for example, in which 1-dimensional channels are enclosed by $[SmCl_9]^{6-}$ tricapped trigonal prisms to provide a short jumping distance of 2.08 Å between two octahedra for Li^+ ion hopping. The fast Li^+ diffusion along the channels is verified through ab initio molecular dynamics simulations. Similar to zeolites, the $SmCl_3$ framework can be grafted with halide species to obtain mobile ions without altering the base structure, achieving an ionic conductivity over 10^{-4} S cm^{-1} at 30 °C with LiCl as the adsorbent. Moreover, the universality of the interface-bonding behavior and ionic diffusion in a class of framework materials is demonstrated. It is suggested that the ionic conductivity of the MCl_3/halide composite (M = La−Gd) is likely in correlation with the ionic conductivity of the grafted halide species, interfacial bonding, and framework composition/dimensions. This work reveals a potential class of halide structures for superionic conductors and opens up a new frontier for constructing zeolite-like frameworks in halide-based materials, which will promote the innovation of superionic conductor design and contribute to a broader selection of halide SSEs.

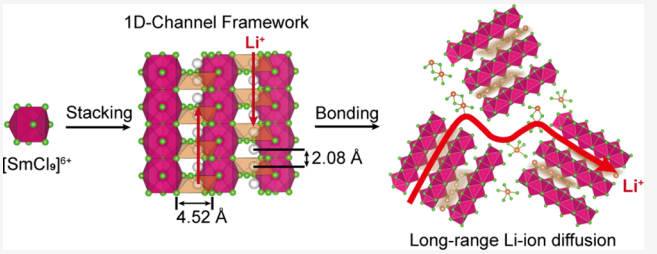

INTRODUCTION

The booming market of electric vehicles today hinges on state-of-the-art energy storage technologies; especially, their durability and safety are priorities.[1] All-solid-state Li^+ ion batteries (ASSLIBs) are a potential candidate due to their high energy density and instinct safety derived from low flammability,[2] but the gap between laboratory demonstration and industrial applications remains large.[3] Recently, the revival of ternary halides with Li−M−Cl (M = Y, Er, In, Zr, etc.) as solid-state electrolytes (SSEs) shows promise in closing the gap due to their favorable room-temperature ionic conductivity and compatibility toward high-voltage cathodes.[4−10] A wide range of halide synthesis routes, including water-mediated synthesis[5] and ammonia-assisted synthesis,[11] are available to meet different production needs. Among the increasingly reported Li−M−Cl SSEs since the first report of Li_3YCl_6 by Tetsuya Asano et al.,[4] such as Li_3InCl_6,[5] Li_2ZrCl_6,[12,13] Li_xScCl_{3+x},[6,10] Li_3ErCl_6,[14] etc.,[15,16] they all share a similar structural pattern. The ionic radii of the metal atoms in Li−M−Cl are close, such as Li^+ (76 pm), In^{3+} (80 pm), Sc^{3+} (74.5 pm), Zr^{4+} (72 pm), and Y^{3+} (90 pm) according to the Shannon−Prewitt effective ionic radius.[17] Within this range of ionic radii, metal halides form $[MCl_6]^{x-}$ octahedra with anionic cubic closest packed or hexagonal closest packed stacks, generating a tetrahedron-assisted lithium-ion diffusion pathway (such as octahedron−tetrahedron−octahedron).[18−20] Beyond these, a few halides with other metallic elements have been reported to have high ionic conductivities so far. We believe that there are potential ion-conducting structures that might have been overlooked.

If the ionic radius of the immobile metal elements in the chloride electrolytes further increases, the metal−halide polyhedra in the structure will transition from sixfold coordination to eightfold or ninefold coordination. There is an interesting group of rare-earth halides MCl_3 (M = La−Sm) with ninefold coordination as shown in Figure 1a, in which

Received: September 5, 2022
Published: December 30, 2022

https://doi.org/10.1021/jacs.2c09446
J. Am. Chem. Soc. 2023, 145, 2183−2194

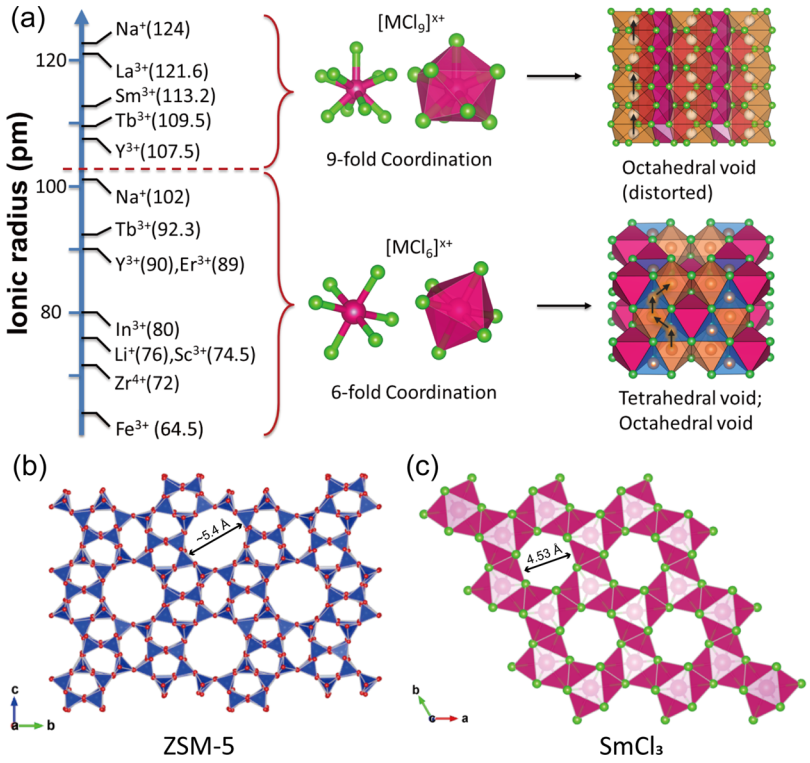

Figure 1. Porous framework structure based on halides. (a) Relationship between the ionic radius of M and the coordination of $[MCl_x]$ polyhedra. The black arrows on the crystal structures indicate the Li^+ diffusion pathway. (b) Crystal lattice of a typical zeolite material, ZSM-5, with a pore size of ~5.4 Å. (c) Top view of the $SmCl_3$ lattice along the *c* axis to show the existing plentiful channels with an inner diameter of 4.53 Å.

MCl_3 forms a $P6_3/m$ lattice with 1-dimensional (1D) channels of vacancies along the *c* axis. It is worth noting that these abundant channels have a similar pore size to those of zeolites, potentially forming a framework for ion diffusion. Other framework materials such as metal−organic frameworks and zeolites have shown great promise for the fabrication of high-performance SSEs through introducing free Li^+, Na^+, or Mg^{2+} ions,[21−25] presenting decent ionic conductivities. Benefiting from the rich porosity, controllable functionality, and modularity, framework materials provide an ideal platform for designing fast ionic conductors. Dated back to 1994, $Na_{3x}M_{2-x}Cl_6$ (M = La−Sm, $P6_3/m$) was reported by Lissner et al.,[26] where Na^+ ions partially occupy the M site, and the rest of the Na^+ ions are located in the channel vacancy sites. These abundant connected octahedral voids provide a short ion jumping distance, accommodating fast sodium diffusion.[27] However, the reported Na^+ conductivity[27] was still well below the requirement for practical application (>10^{-4} S/cm). As for Li^+ diffusion, to the best of our knowledge, no stable Li analogues of $Li_{3x}M_{2-x}Cl_6$ have been reported so far due to the large mismatch between the ionic radii of Li^+ (76 pm) and M^{3+} in MCl_3 (M = La−Sm, 122−113 pm). The possibility of Li^+ diffusion in halide-based framework materials has not been addressed. We believe that Li^+ ions could be highly mobile in the channels of the halide frameworks without altering the framework structure, potentially achieving high Li^+ conductivity.

In this work, the Li^+ diffusion in the $SmCl_3$ framework was studied for the first time through a combination of theoretical calculations and experiments. The $SmCl_3$ lattice with topologies akin to inorganic zeolites is presented in Figure 1b,c, where the 1D hexagonal channels along the *c* axis with an inner diameter of ~4.53 Å are comparable with the typical zeolite ZSM-5 with a nanopore size of ~5.4 Å. The ab initio molecular dynamics (AIMD) simulations confirmed the fast Li^+ diffusion in the 1D channels. Experimentally, the ball-milling (BM)-synthesized $SmCl_3$·0.5LiCl composite (BM-$SmCl_3$·0.5LiCl) exhibited a drastic difference in Li^+ conductivity (~1 × 10^{-4} S/cm) compared to the co-melting (CM)-synthesized composite (CM-$SmCl_3$·0.5LiCl) and ball-milled LiCl (BM-LiCl) (both ~10^{-8} S/cm) at 30 °C. The long-range and short-range structures of the ball-milled samples were systematically studied by X-ray diffraction (XRD), pair distribution function (PDF), and extended X-ray absorption fine structure (EXAFS). Results suggested that the $SmCl_3$ cluster with grafted LiCl cover is responsible for the high conductivity. The mechanism was further confirmed through an electronic structure study via X-ray photoelectron spectroscopy (XPS) and X-ray absorption spectroscopy (XAS). The relationship between ionic diffusion behaviors and the bound state of the $SmCl_3$ framework was studied by in situ XRD and nuclear magnetic resonance (NMR) analyses. Moreover, the universality of the interfacial bonding behavior and ionic diffusion of the class of frameworks was demonstrated, presenting ionic conductivities ranging from 10^{-6} to 10^{-3} S/cm. All-solid-state batteries using an $SmCl_3$ framework-based SSE demonstrated excellent electrochemical performances at room temperature (RT). This work reveals a new promising class of halide structures for fast Li^+ conductors. The systematic study of the formation and ion diffusion mechanisms shall broaden the horizon of superionic conductor design and contribute to a wider selection of SSEs.

https://doi.org/10.1021/jacs.2c09446
J. Am. Chem. Soc. 2023, 145, 2183−2194

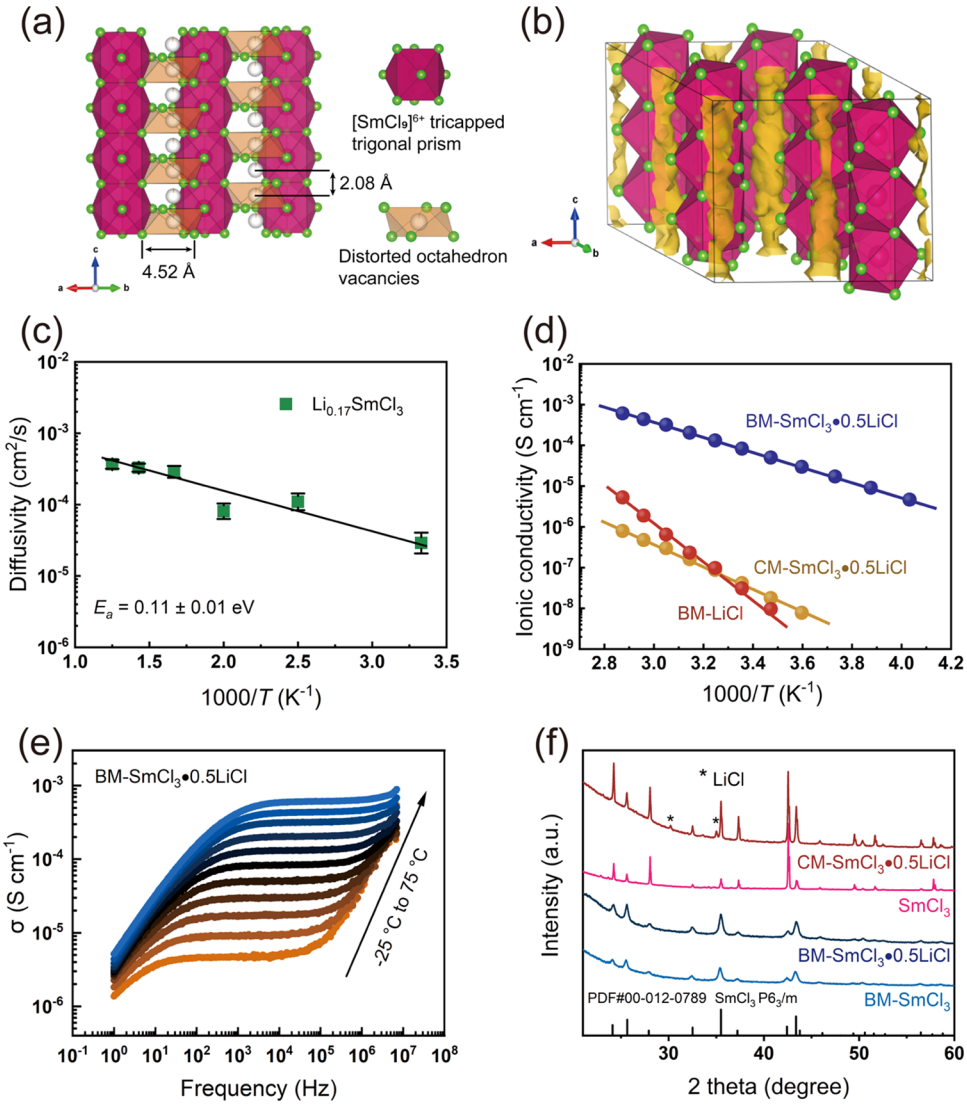

Figure 2. Theoretical calculations and experimental results of ionic diffusion in the $SmCl_3$ halide system. (a) Demonstration of the Li^+ diffusion pathway in $SmCl_3$, with possible Li^+ sites indicated as white balls. (b) Crystal structure of $SmCl_3$ superimposed with Li^+ probability density (yellow iso-surface) from AIMD simulations of $Li_{0.17}SmCl_3$ at 300 K. (c) Arrhenius plot of Li^+ diffusivity from AIMD simulations of $Li_{0.17}SmCl_3$. (d) Arrhenius plots of the BM-$SmCl_3$·0.5LiCl, CM-$SmCl_3$·0.5LiCl, and BM-LiCl. (e) Conductivity isotherms $\sigma(\nu)$ of the as-prepared BM-$SmCl_3$·0.5LiCl SSE recorded at different temperatures. (f) XRD patterns of BM-$SmCl_3$·0.5LiCl, CM-$SmCl_3$·0.5LiCl, $SmCl_3$, and BM-$SmCl_3$.

RESULTS AND DISCUSSION

$SmCl_3$ has a UCl_3-type structure ($P6_3/m$) with the Cl and Sm atoms occupying 6h and 2c Wyckoff sites, respectively. The Sm is coordinated by nine Cl to form tricapped trigonal prisms of $[SmCl_9]^{6-}$. The edge-sharing $[SmCl_9]^{6-}$ polyhedra enclose 1D channels of octahedral voids along the *c* axis direction. The $SmCl_3$ lattice with topologies akin to inorganic zeolites was presented in Figure 1b,c. The 1D hexagonal channels along the *c* axis are clearly shown in Figure 2a with an inner diameter of ~4.52 Å and a short distance of ~2.08 Å between two adjacent cation vacancies. To investigate the ionic diffusion in the 1D channels, we performed AIMD simulations on the model system of $Li_{0.17}SmCl_3$ by incorporating Li into the vacant sites of $SmCl_3$ (see Methods for details). The AIMD simulations reveal fast Li^+ diffusion in the 1D diffusion channels, as shown in the probability density of Li^+ during AIMD simulation (Figure 2b). The Li ions migrate between equivalent distorted octahedral sites through a shared triangle bottleneck as observed in the trajectories of AIMD simulations, showing a low diffusion barrier of 0.11 ± 0.01 eV in the Arrhenius plot (Figure 2c).

Given such a fast ionic diffusion in theoretical study, we have conducted both CM and BM methods to synthesize a Li-containing $SmCl_3$ framework; LiCl was chosen to provide Li^+ ions for the $SmCl_3$ framework, and products are hence for the denoted CM-$SmCl_3$·*x*LiCl and BM-$SmCl_3$·*x*LiCl (see Methods for details). As shown in Figures S1 and S2, the highest ionic conductivity was achieved with BM-$SmCl_3$·0.5LiCl. Interestingly, the BM-$SmCl_3$·0.5LiCl exhibited a Li^+ conductivity (1.2×10^{-4} S/cm) significantly higher than that of BM-LiCl (1×10^{-8} S cm^{-1}) and CM-$SmCl_3$·0.5LiCl (3.1×10^{-8} S cm^{-1}) at 30 °C. Their Arrhenius plots were shown in Figure 2d. The ionic transport in BM-$SmCl_3$·0.5LiCl was reflected by the dispersive regime (Figure 2e) at higher frequencies with a fitted *n* value of 1 according to Jonscher's power law ($\sigma(\omega) = \sigma_{dc} + A\omega^n$), indicating that the ionic diffusion (hopping transition) is probably the dominant contributor to the conductivity.[28−30] The corresponding Nyquist plots and fitted

https://doi.org/10.1021/jacs.2c09446
J. Am. Chem. Soc. 2023, 145, 2183−2194

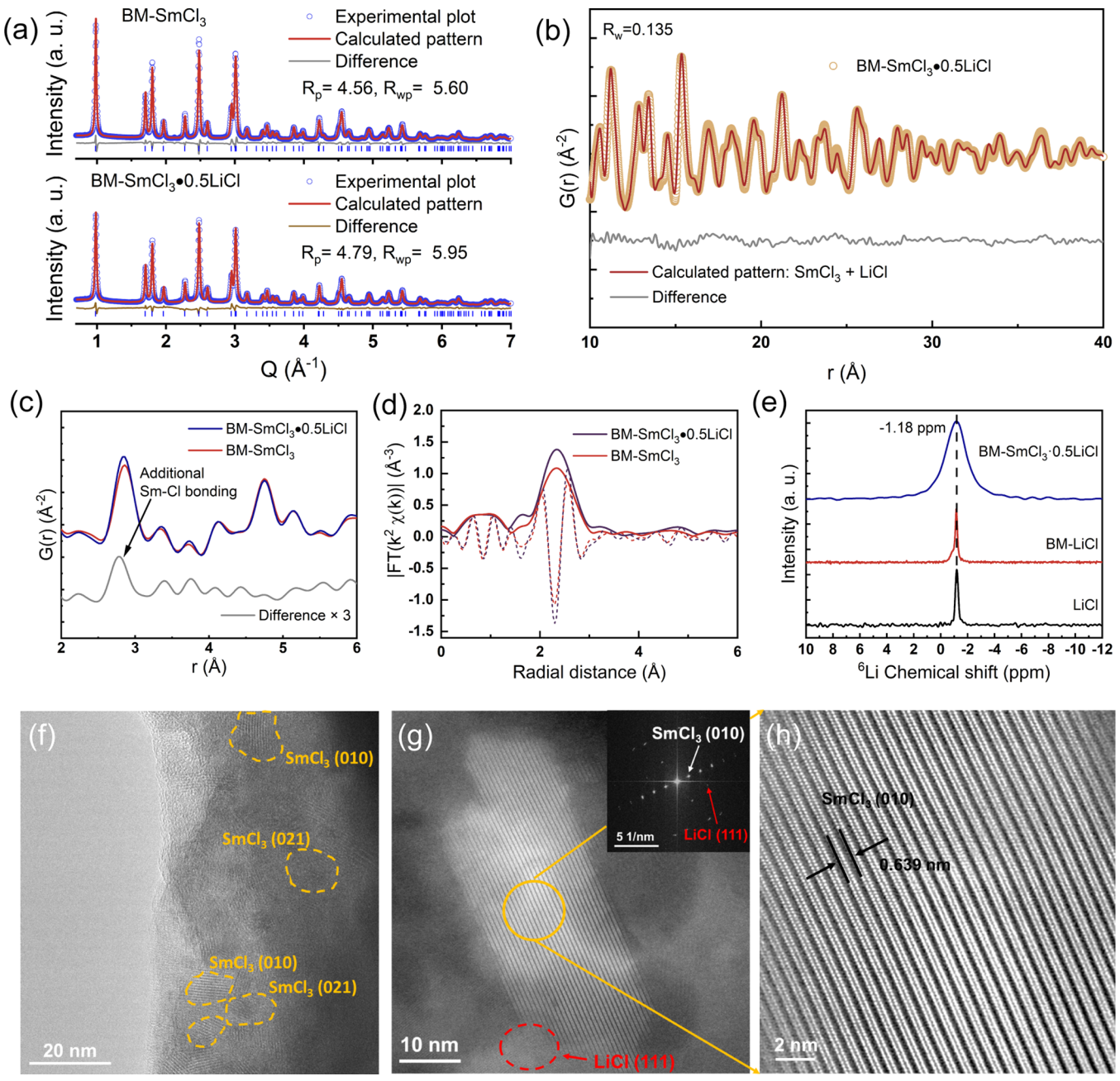

Figure 3. Structure determination of BM-$SmCl_3$·0.5LiCl. (a) Synchrotron-based XRD results and the Rietveld refinements: BM-$SmCl_3$ (top) and BM-$SmCl_3$·0.5LiCl (bottom). (b) Pair distribution function and fitting results of BM-$SmCl_3$·0.5LiCl. (c) Differential pair distribution function curve of BM-$SmCl_3$ and BM-$SmCl_3$·0.5LiCl with the difference between the two curves as shown in the bottom. (d) Fourier transform of the Sm L_3-edge EXAFS in *R*-space, with a k^2-weighing. (e) ^{6}Li MAS NMR spectra of BM-$SmCl_3$·0.5LiCl, BM-LiCl, and LiCl. (f) HRTEM image taken from the particle edge of BM-$SmCl_3$·0.5LiCl. (g) Representative HR-HAADF-STEM images of the crystalline $SmCl_3$ region. The inset figure is a fast Fourier transform image of the digitized TEM image. (h) Enlarged lattice fringes of $SmCl_3$ grains in (g).

curve at 25 °C for the BM-$SmCl_3$·0.5LiCl are shown in Figure S3. The electronic conductivity of BM-$SmCl_3$·0.5LiCl was determined to be sufficiently low (2.49×10^{-9} S cm^{-1}) via chronoamperometry measurements (Figure S4). As presented in the XRD patterns of prepared materials (Figure 2f), both BM-$SmCl_3$·0.5LiCl and CM-$SmCl_3$·0.5LiCl presented a majority phase of $P6_3/m$, except that crystalline LiCl was detected in the CM-$SmCl_3$·0.5LiCl (marked as "*"). Since Li-ions are too small to stay in the Sm site, it is reasonable to observe a LiCl phase segregation after heat treatment. Unlike recently reported Li−M−Cl SSEs that generate a new crystal structure, both CM-$SmCl_3$·0.5LiCl and BM-$SmCl_3$·0.5LiCl preserve the framework structure ($P6_3/m$, UCl_3 type) of $SmCl_3$. Thus, the origin of the difference in ionic conductivities should be the presence or absence of mobile Li^+ ions along the frame channels.

To probe the structural relationship between LiCl and $SmCl_3$ in BM-$SmCl_3$·0.5LiCl, synchrotron-based XRD patterns of the BM-$SmCl_3$ and BM-$SmCl_3$·0.5LiCl were analyzed by Rietveld refinements (Figure 3a). If LiCl reacted with $SmCl_3$ to form a $Li_{2x}(Li_xSm_{2-x})Cl_6$ or a $Li_{3x}(Sm_{2-x}V_x)Cl_6$ crystalline phase, a crystal lattice shrinkage should be expected because

https://doi.org/10.1021/jacs.2c09446
J. Am. Chem. Soc. 2023, 145, 2183−2194

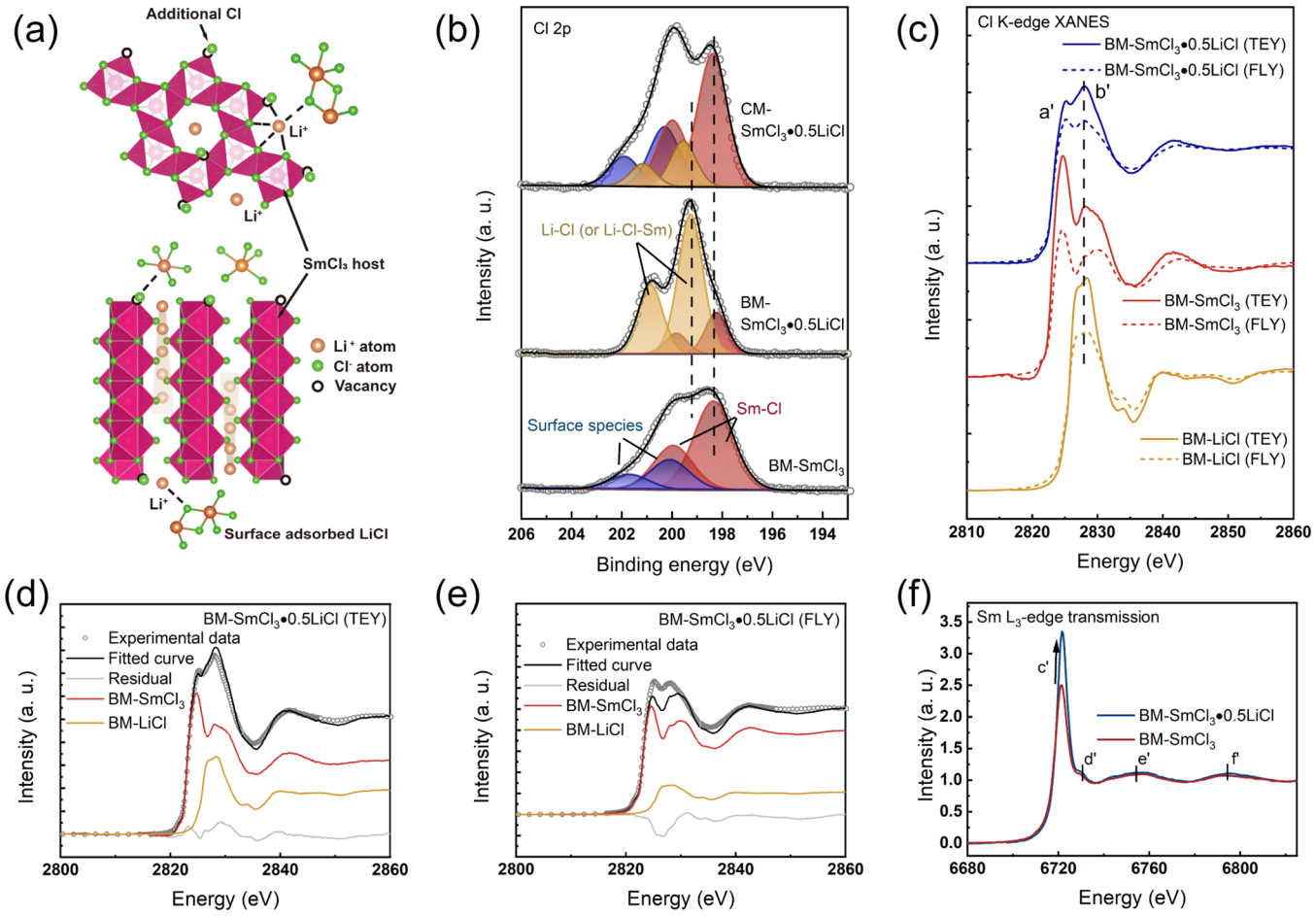

Figure 4. Surface-bulk heterogeneity in BM-$SmCl_3$·0.5LiCl. (a) Schematic host−adsorbent model of LiCl adsorbing onto $SmCl_3$ clusters. (b) Cl 2p XPS spectra of BM-$SmCl_3$, BM-$SmCl_3$·0.5LiCl, and CM-$SmCl_3$·0.5LiCl. (c) XANES region of the Cl K-edge of BM-$SmCl_3$·0.5LiCl, BM-$SmCl_3$, and BM-LiCl in TEY and FLY detect mode. (d,e) Linear combination fitting of BM-$SmCl_3$·0.5LiCl in (d) TEY and (e) FLY. (f) XANES region of the Sm L_3-edge of BM-$SmCl_3$·0.5LiCl and BM-$SmCl_3$ in a transmission mode.

Li^+ is much smaller than Sm^{3+}. However, no obvious difference in lattice parameters can be observed between BM-$SmCl_3$ and BM-$SmCl_3$·0.5LiCl. The accurate unit cell of the BM-$SmCl_3$ sample contained two crystallographic atom positions (Sm1, Cl1) was obtained by Rietveld refinement as shown in Table S1. The unit cell of BM-$SmCl_3$·0.5LiCl was almost identical to that of BM-$SmCl_3$ (Table S2), suggesting that Li^+ did not substitute the Sm^{3+} in the $SmCl_3$ framework. As another counterexample shown in Figure S5, $Na_{0.5}SmCl_{3.5}$ was synthesized through the same BM process, and the XRD pattern presents a shift to the lower angle when compared with BM-$SmCl_3$ and BM-$SmCl_3$·0.5LiCl. A peak splitting at around $2\theta = 44°$ was further observed due to the Na^+ substitution to Sm^{3+}, which was also absent for the BM-$SmCl_3$·0.5LiCl ($Li_{0.5}SmCl_{3.5}$), indicating the diffraction peaks of the BM-$SmCl_3$·0.5LiCl were derived from the intact $SmCl_3$ structure. The average crystallite sizes of BM-$SmCl_3$ and BM-$SmCl_3$·0.5LiCl samples were determined as 32.3 and 30.3 nm in diameter, respectively, according to the Scherrer equation.[17,31] It is worth noting that the long-range ordering of LiCl was also absent in our observation of XRD, as the weight ratio of LiCl in BM-$SmCl_3$·0.5LiCl was below 0.001 according to the Rietveld refinement. It is hard to locate the lithium position and content through the diffraction method.

The total scattering technique coupled with the Fourier transform (FT) and PDF analysis stands out as an effective tool to probe the local structure and quantify the nanophase. Figure 3b and Table S3 display the fits to the experimental PDFs, $G(r)$, of BM-$SmCl_3$·0.5LiCl. Medium-range local structure analysis was carried out using the composite model: $SmCl_3$ ($P6_3/m$) + LiCl (Fm-$3m$) from 10 to 40 Å in real space. The BM-$SmCl_3$·0.5LiCl was fitted well with an R_w = 0.135 using the $SmCl_3$ and LiCl combination model. Quantitatively, the refinements of the $G(r)$ revealed that the fitted weight ratios of $SmCl_3$ (0.923 ± 0.047) and LiCl (0.077 ± 0.047) are well consistent with the stoichiometric weight ratios of $SmCl_3$ (0.924) and LiCl (0.076) raw materials. Combining the synchrotron-based XRD refinements and PDF fitting suggests that the crystallinity of LiCl in the composite was interrupted under mechanical forces and the presence of $SmCl_3$ particles. Differential pair distribution function (d-PDF) analysis (Figure 3c) was conducted within a short range of 6 Å for BM-$SmCl_3$·0.5LiCl and BM-$SmCl_3$ to capture the possible interfacial bonding between $SmCl_3$ and LiCl. The most obvious difference is that BM-$SmCl_3$·0.5LiCl has a more intense peak at 2.85 Å than that of BM-$SmCl_3$, corresponding to the Sm−Cl distance. This can be originated from the bonding between Cl^- of LiCl and the surface-coordinated unsaturated $SmCl_3$ nanocluster. The bonding characteristics of the Sm atoms in $[SmCl_{3+x}]^{x-}$ have been further confirmed by EXAFS analysis. The FT k^2-weighted $\chi(k)$ Sm L_3-edge EXAFS spectra of BM-$SmCl_3$ and BM-$SmCl_3$·0.5LiCl in Figure 3d

https://doi.org/10.1021/jacs.2c09446
J. Am. Chem. Soc. 2023, 145, 2183−2194

demonstrate that the main peak located at $R \cong 2.3$ Å without phase correction should be ascribed to the backscattering from Cl^- coordination. The BM-$SmCl_3$·0.5LiCl has a more intense peak than that of BM-$SmCl_3$ in R space, which is consistent with the d-PDF result. To quantify, we performed the EXAFS Sm−Cl bonding-specific curve-fitting analysis (Figure S6 and Table S4). The average Sm environment in $[SmCl_9]^{6+}$ comprises first-shell Sm−Cl with a coordination number $N = 8.3 \pm 1.2$ and a distance $R = 2.84 \pm 0.01$ Å for BM-$SmCl_3$, and $N = 10.6 \pm 1.3$ and $R = 2.85 \pm 0.01$ Å for BM-$SmCl_3$·0.5LiCl. The Sm−Cl distance derived from EXAFS analysis is in agreement with the distances derived from PDF (2.85 Å) and XRD (2.866 Å) results. Collectively, the increase of coordination number derived from experimental data agrees with the hypothesis that additional Cl^- filled the surface vacancies on $SmCl_3$, strongly suggesting that LiCl bonds to the $SmCl_3$ host rather than resulting from a solid-phase reaction between LiCl and $SmCl_3$.

The composite of LiCl grafted onto the $SmCl_3$ grain was further confirmed by high-resolution transmission electron microscopy (HRTEM) and high-angle annular dark field-scanning transmission electron microscopy (HAADF-STEM) analyses. According to the HRTEM image of BM-$SmCl_3$·0.5LiCl in Figure 3f, the $SmCl_3$ grains were widespread in the particle with random orientations and interconnected by the amorphous region or short-range crystallites. In the HR-HAADF-STEM image of lattice fringes, we identified the representative crystalline region with $(010)_{SmCl3}$ (Figure 3g,h), $(110)_{SmCl3}$ (Figure S8b), and $(111)_{LiCl}$. HR-HAADF-STEM images further suggest that there are crystalline LiCl regions, in addition to amorphous regions (LiCl and/or $SmCl_3$), adjacent to or superimposed on $SmCl_3$ grains. Combining the lattice fringes and spectroscopy analyses, we consider that the connection region should be LiCl and amorphized $SmCl_3$ due to BM treatment.

Both ^{6}Li and ^{7}Li magic-angle spinning (MAS) NMR spectroscopy can be used to investigate the local environment around Li^+ ions. Comparatively, ^{6}Li MAS spectra tend to give a better resolution as ^{6}Li nuclei experience comparatively weaker homonuclear dipole−dipole interactions due to their small magnetogyric ratio. For this reason, ^{6}Li MAS spectra of BM-$SmCl_3$·0.5LiCl and BM-LiCl along with pure solid LiCl were acquired and are shown in Figure 3e. The spectra of the BM-LiCl and the BM-$SmCl_3$·0.5LiCl samples display a strong peak at −1.18 ppm. The chemical shift values are the same as that of solid LiCl, confirming the occurrence of LiCl in BM-$SmCl_3$·0.5LiCl without the formation of Li−Sm−Cl or interference of the $SmCl_3$ framework. The broad signal with low intensity at −0.92 ppm in the BM-LiCl sample implies that some amorphous materials are formed by the mechanical treatment.[32−34] The peak in the spectrum of the BM-$SmCl_3$·0.5LiCl sample is rather broad, indicating a disordered local environment around the LiCl unit, which supports the conclusion derived from the synchrotron-based XRD refinement and the PDF fitting that the crystallinity of the LiCl in the composite has been diminished by mechanical forces.

Here, due to the structural similarity between $SmCl_3$ and zeolites, a host−adsorbent model is proposed as shown in Figure 4a. The long-range crystallinity and chemical bonds of LiCl were interrupted under mechanical forces so that nanocrystalline or amorphous LiCl was grafted to the $SmCl_3$ frame via BM to provide mobile Li^+ ions hopping along the $SmCl_3$ channels. To confirm the adsorption-like mechanism on the surface and interface of $SmCl_3$ clusters, the surface-bulk heterogeneity in the LiCl−$SmCl_3$ composite and electron transfer between LiCl and $SmCl_3$ were revealed by a combined XPS and XAS study. The XPS spectra of Sm 3d and Cl 2p orbitals of BM-$SmCl_3$, BM-$SmCl_3$·0.5LiCl, and CM-$SmCl_3$·0.5LiCl were investigated to reveal the chemical and electronic states of the particle surface. In the Cl 2p spectra (Figure 4b), BM-$SmCl_3$ demonstrated two sets of doublets, depicted with blue peaks and red peaks. The red peaks refer to the subsurface Cl in $SmCl_3$, whereas the shifted blue peaks might be originated from the surface species due to the surface core-level shift.[35,36] After introducing LiCl through BM, a new doublet (yellow peaks) arose and dominated at 199.2 and 200.9 eV in BM-$SmCl_3$·0.5LiCl, which can be assigned to the Li−Cl bonding (or Li−Cl−Sm),[37] suggesting the LiCl surface-enrichment. In CM-$SmCl_3$·0.5LiCl, the surface enrichment of LiCl was reduced, which is consistent with the LiCl−$SmCl_3$ phase separation observed in the previous XRD results. A peak shifting to the lower energy of Sm 3d spectra was observed in BM-$SmCl_3$·0.5LiCl compared to that of BM-$SmCl_3$ and CM-$SmCl_3$·0.5LiCl (Figure S10), which is due to the electron donation from the surface additional Cl^-−Sm^{3+}.

X-ray absorption near edge structure (XANES) can provide a comparison of surface and bulk electronic structure via switching the detection modes between total electron yield (TEY, <10 nm depth) and fluorescence yield (FLY, ∼50−100 nm depth), especially in the soft and tender X-ray region such as the Cl K-edge. Cl K-edge XANES of BM-$SmCl_3$·0.5LiCl, BM-$SmCl_3$, and BM-LiCl are studied via TEY and FLY modes, as shown in Figure 4c with solid lines as TEY-detected and dashed lines as FLY-detected. The pre-edge-feature a′ was assigned to transitions from Cl 1s to the mixing state of Cl 3p and Sm 5d, and feature b′ was assigned to transitions from Cl 1s to the unoccupied Cl 4p-state.[38] The reference BM-$SmCl_3$ has a strong pre-edge signal due to the Sm−Cl hybridization, whereas BM-LiCl only presents a main transition feature b′. Both BM-$SmCl_3$ and BM-LiCl look similar in TEY mode and FLY mode except for the intensity shrinkage due to the self-absorption effect. As expected, BM-$SmCl_3$·0.5LiCl demonstrated different features in TEY mode and FLY mode. The rising edge b′ of BM-$SmCl_3$·0.5LiCl is much stronger in TEY than in FLY, indicating a higher LiCl concentration on the surface. Quantitative analysis of the composite component of BM-$SmCl_3$·0.5LiCl was studied through linear combination fitting with BM-$SmCl_3$ and BM-LiCl, as shown in Figure 4d,e. From surface to bulk, the LiCl contribution was reduced from 36 to 20% (theoretically, it should be ∼15% for a uniform distribution), confirming that LiCl covered the $SmCl_3$ surface to form a core−shell-like structure. In the Sm L_3-edge XANES of transmission detected mode, four different characteristic peaks are marked as c′, d′, e′, and f′. The rising edge feature c′ and feature d′ originated from electric-dipole allowing transitions from Sm 2p-orbitals to unoccupied states that contain Sm 5d character ($2p^64f^65d^0 \rightarrow 2p^54f^65d^1$ transitions). Features e′ and f′ can be assigned to the multiple scattering resonance or the transition to quasi-bound states.[39] Interestingly, relative to the BM-$SmCl_3$, the BM-$SmCl_3$·0.5LiCl has a noticeable sharper white line a′ just above the threshold (Figure 4f). The Sm L_3-edge XANES in transmission reveals an increase in the density of unoccupied 5d states (a bulk effect), i.e., loss of electrons, which is contrary to surface Sm 3d XPS results (gain of electrons) for BM-$SmCl_3$·0.5LiCl. This contradiction can be explained by the surface-bulk hetero-

https://doi.org/10.1021/jacs.2c09446
J. Am. Chem. Soc. 2023, 145, 2183−2194

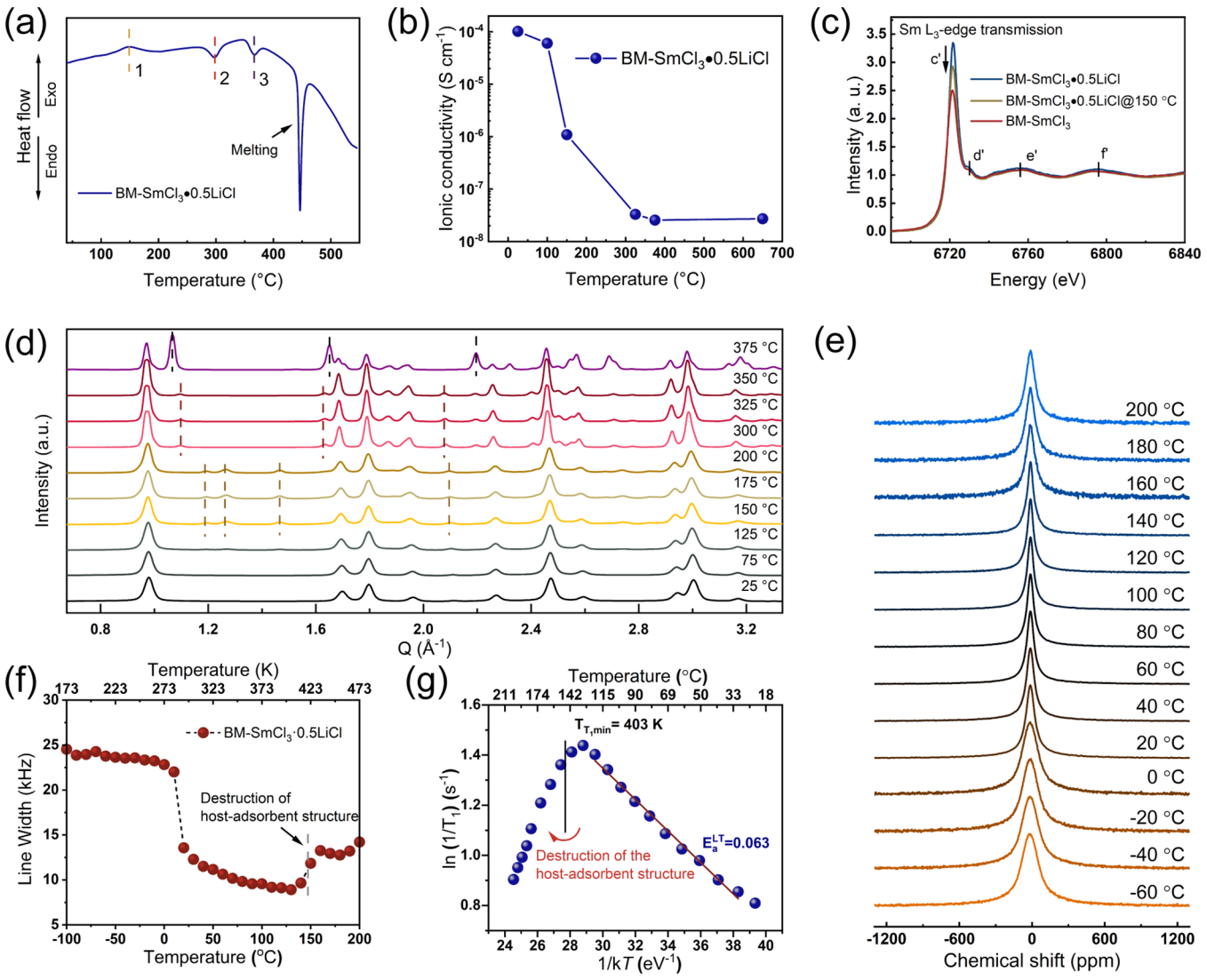

Figure 5. Temperature-dependent ionic diffusion behaviors in BM-$SmCl_3$·0.5LiCl. (a) DSC curve of the BM-$SmCl_3$·0.5LiCl. (b) Ionic conductivities of BM-$SmCl_3$·0.5LiCl annealed at different temperatures for 10 h. (c) XANES region of the Sm L_3-edge of BM-$SmCl_3$, BM-$SmCl_3$·0.5LiCl, and BM-$SmCl_3$·0.5LiCl@150 °C (annealed at 150 °C for 10 h) in transmission mode. (d) In situ XRD results of BM-$SmCl_3$·0.5LiCl at elevated temperatures. (e) Temperature dependence of the ^{7}Li NMR spectra of BM-$SmCl_3$·0.5LiCl observed at various temperatures ranging from −60 to 200 °C. (f) Motional narrowing of the line width of the ^{7}Li NMR central transition of the BM-$SmCl_3$·0.5LiCl sample. The rigid-lattice regime is reached at a temperature lower than 283 K (10 °C). (g) Temperature dependence of diffusion-induced ^{7}Li NMR SLR rates in the laboratory frame of reference for BM-$SmCl_3$·0.5LiCl. The Larmor frequency is 155.2 MHz.

geneity due to the LiCl bonding to the surface of $SmCl_3$ nanoparticles, generating an $[SmCl_{3+x}]^{x-}$ negative-charged framework and surface Li^+ ions. The combination of XPS and XAS has confirmed a core−shell-like structure of BM-$SmCl_3$·0.5LiCl, supporting the host−adsorbent model.

The morphologies of $SmCl_3$, BM-$SmCl_3$, BM-$SmCl_3$·0.5LiCl, and CM-$SmCl_3$·0.5LiCl were present in Figure S14. The BM process significantly reduces the particle size of $SmCl_3$ from the micron-scale (pristine $SmCl_3$) to the nanoscale (BM-$SmCl_3$). Interestingly, the BM-$SmCl_3$·0.5LiCl presents different morphological characteristics, which have a smooth surface and are well-connected between different particles. LiCl appears to "coat" onto the $SmCl_3$ particles to help build a well-connected network. As for the CM method, large particles with fractures were generated again in CM-$SmCl_3$·0.5LiCl. We believed that the LiCl is separated from $SmCl_3$ according to the XRD results. In the Raman spectra of Figure S15, a strong fluorescent signal was presented in the BM samples, whereas it was absent in pristine $SmCl_3$ and CM-$SmCl_3$·0.5LiCl. One possible reason is that the BM process creates abundant surface defects on $SmCl_3$ nanoparticles, giving rise to a strong fluorescent signal. We presume that the surface defects of $SmCl_3$ provide anchoring sites for LiCl.

The relationship between ionic diffusion behaviors and the host−adsorbent state was further studied. The differential scanning calorimetry (DSC) results of BM-$SmCl_3$·0.5LiCl are shown in Figure 5a. A sharp endothermal peak at 445 °C refers to the melting process of BM-$SmCl_3$·0.5LiCl. Before the melting point, there are one exothermal peak and two endothermal peaks at around 150, 300, and 360 °C, respectively, suggesting that several metastable phases existed. Figure 5b shows ionic conductivities after annealing the BM-$SmCl_3$·0.5LiCl at different temperatures for 10 h. The ionic conductivity of the annealed sample significantly decreased

https://doi.org/10.1021/jacs.2c09446
J. Am. Chem. Soc. 2023, 145, 2183−2194

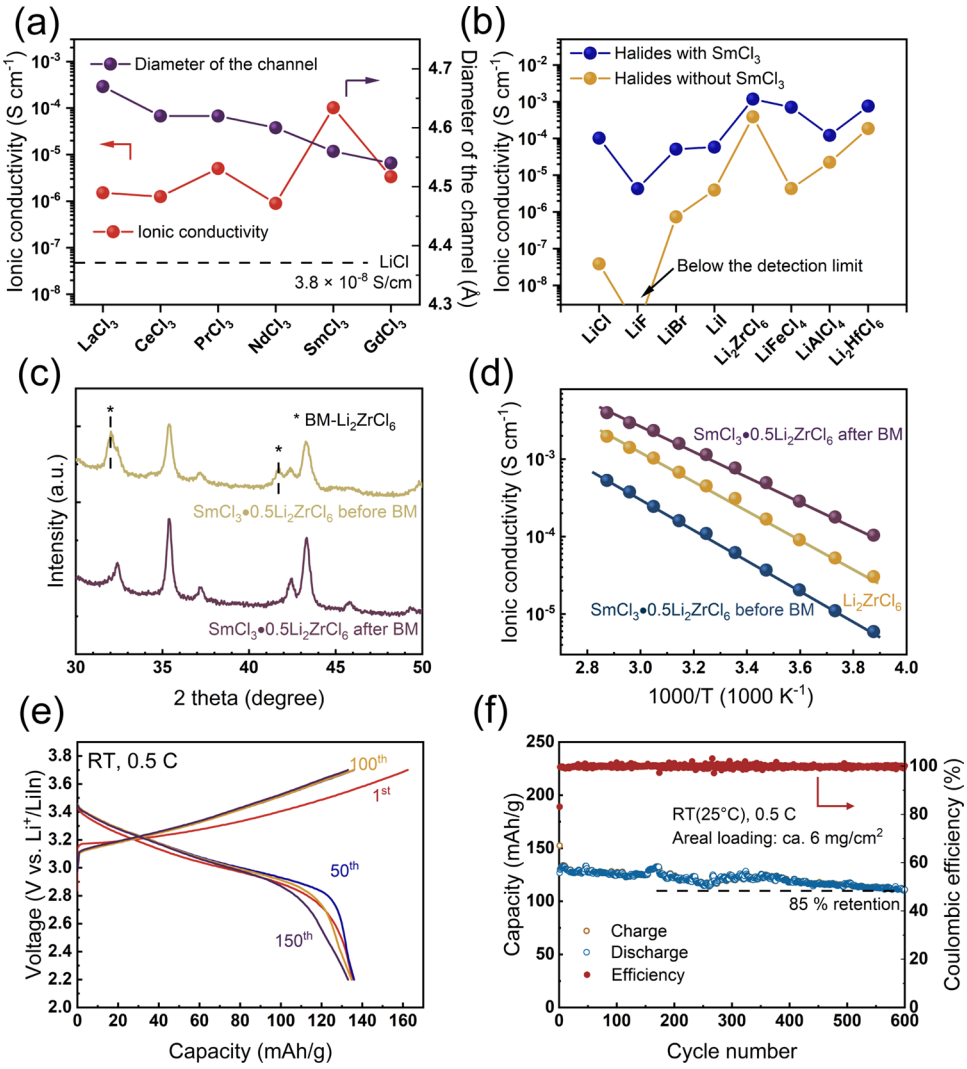

Figure 6. Demonstration of the universality of ionic diffusion behavior in the $SmCl_3$ framework and battery performance. (a) Ionic conductivities of different frameworks MCl_3 (M = La, Ce, Pr, Nd, and Gd) coupled with 0.5 LiCl (molar ratio) at 30 °C. (b) Ionic conductivities of the $SmCl_3$ framework coupled with different halide adsorbents at 30 °C. (c) XRD patterns of the $SmCl_3{\cdot}0.5Li_2ZrCl_6$ before and after ball-milling. (d) Arrhenius-plots of Li_2ZrCl_6 and the $SmCl_3{\cdot}0.5Li_2ZrCl_6$ (before and after ball-milling). (e) Charge and discharge voltage profiles of the ASSLIB using $LiNi_{0.83}Mn_{0.06}Co_{0.11}O_2$ (NMC83) as the cathode and $SmCl_3{\cdot}0.5Li_2ZrCl_6$ as the SSE layer at different cycles (1st, 50th, 100th, and 150th). (f) Plots of capacity and Coulombic efficiency vs cycling numbers of the ASSLIB in (e).

once the annealing temperature was higher than 150 °C, corresponding to the first exothermal peak. The decrease of rising edge feature c′ of the Sm L_3-edge of BM-$SmCl_3{\cdot}$ 0.5LiCl@150 °C in Figure 5c indicates the possible destruction of the bound state between $SmCl_3$ and LiCl. In situ temperature-dependent XRD (Figure 5d) was studied to determine the presence of metastable phases. As the temperature increased, three metastable crystal phases were detected in a sequence, namely, α-Li−Sm−Cl, β-Li−Sm−Cl, and γ-Li−Sm−Cl, matching well with DSC results. It is hard to identify the three metastable crystal phases since no Li−Sm−Cl structures have been reported so far. However, the results still revealed that the fast ionic diffusion is directly related to the bound state of LiCl. Once the bound state was damaged along with the formation of crystalline Li−Sm−Cl, the loss of movable lithium ions in the channel give rise to a decrease in ionic conductivity.

The evolution of Li^+ dynamics is further examined by motional narrowing studies of the ^7Li static NMR spectra of BM-$SmCl_3{\cdot}$0.5LiCl. Figure 5e,f shows that the static ^7Li NMR spectra were obtained in a temperature range from −100 to 200 °C. The changes in the linewidth as a function of temperature were identified in three regions qualitatively in Figure 5e visually and quantitatively in Figure 5f. At lower temperatures (below 0 °C), the full width at half-maximum (FWHM) was large and dominated by the dipolar coupling of the nuclear spins of ^7Li achieving the rigid-lattice regime. At 0 °C, a sudden decrease in FWHM was observed. The abrupt change in FWHM at 0 °C was due to the fact that the Li−Li dipolar interactions were drastically averaged by thermally activated motions of Li ions, i.e., the rapid Li^+ diffusions. Between 0 and 140 °C, the FWHM gradually decreased with increasing temperature. Interestingly, when the temperature was above 140 °C, an increase in FWHM with increasing temperature was observed. The FWHM within the temperature between 160 and 200 °C was around 14 kHz. This abnormal thermal behavior is consistent with the in situ XRD result that the material undergoes a phase transition to a

https://doi.org/10.1021/jacs.2c09446
J. Am. Chem. Soc. 2023, 145, 2183−2194

metastable phase with lower Li^+ diffusion rates at elevated temperatures above 150 °C.

The temperature-dependent ^7Li static spin−lattice relaxation (SLR) rates in the laboratory frame of reference ($1/T_1$) were measured to determine activation energies of lithium-ion diffusions as the $1/T_1$ is directly related to the spectral density function of the Li^+ jumping process.[40,41] As shown in Figure 5g, below the phase transition temperature (150 °C), a $1/T_1$ maximum was reached at 130 °C, and the ln ($1/T_1$) versus temperature (T) plot satisfied an Arrhenius behavior in the low-temperature regime. The activation energy of the low-temperature flank (E_a^{LT}) was determined as low as 0.063 eV for the BM-$SmCl_3$·0.5LiCl sample, corresponding to the short-range Li^+ diffusion, which is in agreement with the estimated energy barrier in AIMD simulations (Figure 2c). In the laboratory frame of reference, an absolute lithium jump rate can be deduced from the maximum condition ($\tau \cdot \omega_o \approx 1$) at the relaxation rate peak, where the τ represents the average correlation time/residence time between subsequent hops.[42−45] Considering this condition, the Larmor frequency of $\omega_0/(2\pi)$ = 155.2 MHz results in a Li^+ jump frequency/jump rate (τ^{-1}) of 9.8 × 10^8 s^{-1} at 403 K. It is reported that the residence time τ in the ns regime corresponds to an ionic conductivity on the order of 10^{-3} S cm^{-1},[43,46] implying a reasonable conductivity at 130 °C.

The above-shown data clearly show that the bound state between $SmCl_3$ crystalline and grafted LiCl is responsible for the fast ionic diffusion. However, even for BM-$SmCl_3$·0.5LiCl, the ionic conductivity is still 2 to 3 orders of magnitude below the theoretically calculated value of the framework. We consider that there should be other factors influencing ion transport. For example, diffusion within 1D channels severely depends on lattice continuity. The fast ion diffusion according to the theoretical calculation would be compromised due to lattice mismatch in practical cases. Thus, the grafted LiCl between different $SmCl_3$ domains is not only a provider of mobile Li^+ but also an important ion conduction path between the mismatched $SmCl_3$ clusters. The poor diffusion properties of LiCl reduce inter-grain diffusion and make it a rate-limiting step. Moreover, the ratio of interface region in the composite also affects the ionic conductivity. The ionic conductivities upon different BM conditions (Figure S2) and corresponding nano-structural analyses (Figure S16) demonstrated that the ionic conductivity is correlated with the domain size of the $SmCl_3$.

We also replaced $SmCl_3$ in BM-$SmCl_3$·0.5LiCl with MCl_3 (M = La, Ce, Pr, Nd, Gd) to demonstrate the universality of ionic diffusion behaviors in the host−adsorbent structure. All of them show similar channel sizes and presented faster Li^+ diffusion than that of pure LiCl, as shown in Figure 6a. We further replace the LiCl in BM-$SmCl_3$·0.5LiCl with LiF, LiBr, LiI, or even Li−M−Cl, such as $LiFeCl_4$, Li_2ZrCl_6, and $LiAlCl_4$ (Figure 6b). The comparison between samples with and without $SmCl_3$ confirmed the boosting effect of $SmCl_3$ on the ionic conductivity of the composites. The corresponding diffraction signal of adsorbents disappeared in the composite after BM treatment (Figures S19 and S20). Taking the $SmCl_3$·0.5Li_2ZrCl_6 as an example, the diffraction peaks of BM-Li_2ZrCl_6 disappeared after BM with $SmCl_3$ (Figure 6c), indicating the interruption of its crystallinity due to the coating form onto the $SmCl_3$ nanoparticles. After BM, its ionic conductivity increased by ∼10 times compared to that before BM, even higher than the pure Li_2ZrCl_6 SSE (Figure 6d). The application potential of the $SmCl_3$ framework-based SSEs was demonstrated by constructing ASSLIBs using BM-$SmCl_3$·0.5Li_2ZrCl_6 as the SSE layer. $LiNi_{0.83}Mn_{0.06}Co_{0.11}O_2$ (NMC83) was selected as a cathode active material for ASSLIB evaluations, and detailed cell configurations were described in the Methods. The ASSLIB with BM-$SmCl_3$·0.5Li_2ZrCl_6 as the SSE layer exhibited excellent cycle performance under 0.5C (1C = 200 mAh g^{-1}) in a voltage range of 2.2−3.7 V (vs Li^+/LiIn). The charge−discharge curves in Figure 6e depicted a high reversible charge−discharge process and lower voltage decay at the 1st, 50th, 100th, and 150th cycles, respectively. As shown in Figure 6f, the ASSLIB with BM-$SmCl_3$·0.5Li_2ZrCl_6 SSE demonstrated highly stable cycling performance for over 600 cycles with a capacity retention of 85%.

CONCLUSIONS

In summary, we reported a new class of zeolite-like halide frameworks, $SmCl_3$, for example, in which 1D channels were enclosed by $[SmCl_9]^{6-}$ tricapped trigonal prisms, providing a short jumping distance of 2.08 Å between vacancies for Li^+ hopping. The fast Li^+ diffusion along the channels was verified through AIMD calculations and in situ NMR measurements. Combining the structure and bonding analysis, we propose a zeolite-like host−adsorbent structure prepared by a BM process, generating delocalized Li^+ ions moving through the 1D channels in the $SmCl_3$ framework. The ionic conductivities of the BM-$SmCl_3$·0.5LiCl and BM-$SmCl_3$·0.5Li_2ZrCl_6 SSEs are over 10^{-4} S cm^{-1} and 10^{-3} S cm^{-1} at 30 °C, respectively. Moreover, the interfacial bonding behavior and ionic diffusion of the class of frameworks were demonstrated to be universal across different halides, presenting ionic conductivities ranging from 10^{-6} to 10^{-3} S/cm. It is suggested that the ionic conductivity of the MCl_3/halide composites (M = La-Gd) is likely in correlation with the ionic conductivity of grafted halide species, interfacial bonding, and framework composition/dimensions. This work reveals a potential class of structures in halides for fast superionic conductors, which will broaden the horizon of superionic conductor design and contribute to a wider selection of halide SSEs.

ASSOCIATED CONTENT

Supporting Information

The Supporting Information is available free of charge at https://pubs.acs.org/doi/10.1021/jacs.2c09446.

Complete experimental details, characterization details, ab initio molecular dynamics simulations, and additional figures (PDF)

AUTHOR INFORMATION

Corresponding Authors

Tsun-Kong Sham − *Department of Chemistry, University of Western Ontario, London, Ontario N6A 5B7, Canada;* orcid.org/0000-0003-1928-6697; Email: tsham@uwo.ca

Yifei Mo − *Department of Materials Science and Engineering, University of Maryland, College Park, Maryland 20742, United States;* orcid.org/0000-0002-8162-4629; Email: yfmo@umd.edu

Xueliang Sun − *Department of Mechanical and Materials Engineering, University of Western Ontario, London, Ontario N6A 5B9, Canada;* orcid.org/0000-0003-0374-1245; Email: xsun9@uwo.ca

https://doi.org/10.1021/jacs.2c09446
J. Am. Chem. Soc. 2023, 145, 2183−2194

Authors

Jiamin Fu − *Department of Mechanical and Materials Engineering, University of Western Ontario, London, Ontario N6A 5B9, Canada; Department of Chemistry, University of Western Ontario, London, Ontario N6A 5B7, Canada*

Shuo Wang − *Department of Materials Science and Engineering, University of Maryland, College Park, Maryland 20742, United States*

Jianwen Liang − *Department of Mechanical and Materials Engineering, University of Western Ontario, London, Ontario N6A 5B9, Canada*

Sandamini H. Alahakoon − *Department of Chemistry, University of Western Ontario, London, Ontario N6A 5B7, Canada*

Duojie Wu − *Department of Materials Science and Engineering, Southern University of Science and Technology, Shenzhen 518055, China*

Jing Luo − *Department of Mechanical and Materials Engineering, University of Western Ontario, London, Ontario N6A 5B9, Canada*

Hui Duan − *Department of Mechanical and Materials Engineering, University of Western Ontario, London, Ontario N6A 5B9, Canada*

Shumin Zhang − *Department of Mechanical and Materials Engineering, University of Western Ontario, London, Ontario N6A 5B9, Canada; Department of Chemistry, University of Western Ontario, London, Ontario N6A 5B7, Canada*

Feipeng Zhao − *Department of Mechanical and Materials Engineering, University of Western Ontario, London, Ontario N6A 5B9, Canada*

Weihan Li − *Department of Mechanical and Materials Engineering, University of Western Ontario, London, Ontario N6A 5B9, Canada*

Minsi Li − *Department of Mechanical and Materials Engineering, University of Western Ontario, London, Ontario N6A 5B9, Canada*

Xiaoge Hao − *Department of Mechanical and Materials Engineering, University of Western Ontario, London, Ontario N6A 5B9, Canada*

Xiaona Li − *Department of Mechanical and Materials Engineering, University of Western Ontario, London, Ontario N6A 5B9, Canada*

Jiatang Chen − *Chemical Engineering, McMaster University, Hamilton, Ontario L8S 4M1, Canada;* orcid.org/0000-0002-9705-6523

Ning Chen − *Canadian Light Source Inc., University of Saskatchewan, Saskatoon, Saskatchewan S7N 2V3, Canada;* orcid.org/0000-0002-1269-6119

Graham King − *Canadian Light Source Inc., University of Saskatchewan, Saskatoon, Saskatchewan S7N 2V3, Canada;* orcid.org/0000-0003-1886-7254

Lo-Yueh Chang − *National Synchrotron Radiation Research Centre, Hsinchu 30076, Taiwan*

Ruying Li − *Department of Mechanical and Materials Engineering, University of Western Ontario, London, Ontario N6A 5B9, Canada*

Yining Huang − *Department of Chemistry, University of Western Ontario, London, Ontario N6A 5B7, Canada;* orcid.org/0000-0001-9265-5896

Meng Gu − *Department of Materials Science and Engineering, Southern University of Science and Technology, Shenzhen 518055, China;* orcid.org/0000-0002-5126-9611

Complete contact information is available at: https://pubs.acs.org/10.1021/jacs.2c09446

Author Contributions

○J.F., S.W., and J.L. contributed equally to this work.

Notes

The authors declare no competing financial interest.

■ ACKNOWLEDGMENTS

This research was supported by the Natural Sciences and Engineering Research Council of Canada (NSERC), Canada Research Chair Program (CRC), Canada Foundation for Innovation (CFI), Ontario Research Fund, the Canada Light Source at the University of Saskatchewan (CLS), Interdisciplinary Development Initiatives (IDI) by Western University, Canada MITACS fellow, and University of Western Ontario. The authors also appreciate the help of the beamline scientist of HXMA (Dr. Weifeng Chen), VESPERS (Dr. Renfei Feng), PGM (Dr. Lucia Zuin), BXDS, and SXRMB (Dr. Mohsen Shakouri, Dr. Qunfeng Xiao, and Dr. Yongfeng Hu) beamline at Canadian Light Source, 20-BM/ID (Dr. Zou Finfrock, Dr. Debora Motta Meira, and Dr. Michael Pape) at Advanced Photon Source, and 19A (Dr. Yu-Chun Chuang) at Taiwan Photon Source. Y.M. acknowledges the funding support from the US National Science Foundation Award# 1940166 and the computational facilities from the University of Maryland supercomputing resources and the Maryland Advanced Research Computing Center (MARCC). M.G. acknowledges the funding support from Shenzhen Science and Technology Program (Grant no. KQTD20190929173815000) and Guangdong Innovative and Entrepreneurial Research Team Program (Grant no. 2019ZT08C044). The TEM work used the resources of Pico Center from SUSTech Core Research Facilities.

■ REFERENCES

(1) Harper, G.; Sommerville, R.; Kendrick, E.; Driscoll, L.; Slater, P.; Stolkin, R.; Walton, A.; Christensen, P.; Heidrich, O.; Lambert, S.; Abbott, A.; Ryder, K.; Gaines, L.; Anderson, P. Recycling lithium-ion batteries from electric vehicles. *Nature* **2019**, *575*, 75−86.

(2) Sun, Y.-K. Promising All-Solid-State Batteries for Future Electric Vehicles. *ACS Energy Lett.* **2020**, *5*, 3221−3223.

(3) Albertus, P.; Anandan, V.; Ban, C.; Balsara, N.; Belharouak, I.; Buettner-Garrett, J.; Chen, Z.; Daniel, C.; Doeff, M.; Dudney, N. J.; Dunn, B.; Harris, S. J.; Herle, S.; Herbert, E.; Kalnaus, S.; Libera, J. A.; Lu, D.; Martin, S.; McCloskey, B. D.; McDowell, M. T.; Meng, Y. S.; Nanda, J.; Sakamoto, J.; Self, E. C.; Tepavcevic, S.; Wachsman, E.; Wang, C.; Westover, A. S.; Xiao, J.; Yersak, T. Challenges for and Pathways toward Li-Metal-Based All-Solid-State Batteries. *ACS Energy Lett.* **2021**, *6*, 1399−1404.

(4) Asano, T.; Sakai, A.; Ouchi, S.; Sakaida, M.; Miyazaki, A.; Hasegawa, S. Solid Halide Electrolytes with High Lithium-Ion Conductivity for Application in 4 V Class Bulk-Type All-Solid-State Batteries. *Adv. Mater.* **2018**, *30*, No. 1803075.

(5) Li, X.; Liang, J.; Chen, N.; Luo, J.; Adair, K. R.; Wang, C.; Banis, M. N.; Sham, T. K.; Zhang, L.; Zhao, S.; Lu, S.; Huang, H.; Li, R.; Sun, X. Water-Mediated Synthesis of a Superionic Halide Solid Electrolyte. *Angew. Chem., Int. Ed.* **2019**, *58*, 16427−16432.

(6) Zhou, L.; Kwok, C. Y.; Shyamsunder, A.; Zhang, Q.; Wu, X.; Nazar, L. F. A new halospinel superionic conductor for high-voltage all solid state lithium batteries. *Energy Environ. Sci.* **2020**, *13*, 2056−2063.

(7) Jung, S.-K.; Gwon, H.; Yoon, G.; Miara, L. J.; Lacivita, V.; Kim, J.-S. Pliable Lithium Superionic Conductor for All-Solid-State Batteries. *ACS Energy Lett.* **2021**, *6*, 2006−2015.

(8) Park, K.-H.; Kaup, K.; Assoud, A.; Zhang, Q.; Wu, X.; Nazar, L. F. High-Voltage Superionic Halide Solid Electrolytes for All-Solid-State Li-Ion Batteries. *ACS Energy Lett.* **2020**, *5*, 533−539.
(9) Li, X.; Liang, J.; Luo, J.; Norouzi Banis, M.; Wang, C.; Li, W.; Deng, S.; Yu, C.; Zhao, F.; Hu, Y.; Sham, T.-K.; Zhang, L.; Zhao, S.; Lu, S.; Huang, H.; Li, R.; Adair, K. R.; Sun, X. Air-stable Li_3InCl_6 electrolyte with high voltage compatibility for all-solid-state batteries. *Energy Environ. Sci.* **2019**, *12*, 2665−2671.
(10) Liang, J.; Li, X.; Wang, S.; Adair, K. R.; Li, W.; Zhao, Y.; Wang, C.; Hu, Y.; Zhang, L.; Zhao, S.; Lu, S.; Huang, H.; Li, R.; Mo, Y.; Sun, X. Site-Occupation-Tuned Superionic Li_xScCl_{3+x} Halide Solid Electrolytes for All-Solid-State Batteries. *J. Am. Chem. Soc.* **2020**, *142*, 7012−7022.
(11) Wang, C.; Liang, J.; Luo, J.; Liu, J.; Li, X.; Zhao, F.; Li, R.; Huang, H.; Zhao, S.; Zhang, L.; Wang, J.; Sun, X. A universal wet-chemistry synthesis of solid-state halide electrolytes for all-solid-state lithium-metal batteries. *Sci. Adv.* **2021**, *7*, No. eabh1896.
(12) Wang, K.; Ren, Q.; Gu, Z.; Duan, C.; Wang, J.; Zhu, F.; Fu, Y.; Hao, J.; Zhu, J.; He, L.; Wang, C. W.; Lu, Y.; Ma, J.; Ma, C. A cost-effective and humidity-tolerant chloride solid electrolyte for lithium batteries. *Nat. Commun.* **2021**, *12*, 4410.
(13) Kwak, H.; Han, D.; Lyoo, J.; Park, J.; Jung, S. H.; Han, Y.; Kwon, G.; Kim, H.; Hong, S. T.; Nam, K. W.; Jung, Y. S. New Cost-Effective Halide Solid Electrolytes for All-Solid-State Batteries: Mechanochemically Prepared Fe^{3+}-Substituted Li_2ZrCl_6. *Adv. Energy Mater.* **2021**, *11*, No. 2003190.
(14) Schlem, R.; Muy, S.; Prinz, N.; Banik, A.; Shao-Horn, Y.; Zobel, M.; Zeier, W. G. Mechanochemical Synthesis: A Tool to Tune Cation Site Disorder and Ionic Transport Properties of Li_3MCl_6 (M = Y, Er) Superionic Conductors. *Adv. Energy Mater.* **2019**, *10*, No. 1903719.
(15) Zhou, L.; Zuo, T.-T.; Kwok, C. Y.; Kim, S. Y.; Assoud, A.; Zhang, Q.; Janek, J.; Nazar, L. F. High areal capacity, long cycle life 4 V ceramic all-solid-state Li-ion batteries enabled by chloride solid electrolytes. *Nat. Energy* **2022**, *7*, 83−93.
(16) Helm, B.; Schlem, R.; Wankmiller, B.; Banik, A.; Gautam, A.; Ruhl, J.; Li, C.; Hansen, M. R.; Zeier, W. G. Exploring Aliovalent Substitutions in the Lithium Halide Superionic Conductor $Li_{3-x}In_{1-x}Zr_xCl_6$ ($0 \le x \le 0.5$). *Chem. Mater.* **2021**, *33*, 4773−4782.
(17) Shannon, R. Revised effective ionic radii and systematic studies of interatomic distances in halides and chalcogenides. *Acta Crystallogr., Sect. A: Cryst. Phys., Diffr., Theor. Gen. Crystallogr.* **1976**, *32*, 751−767.
(18) Wang, S.; Bai, Q.; Nolan, A. M.; Liu, Y.; Gong, S.; Sun, Q.; Mo, Y. Lithium Chlorides and Bromides as Promising Solid-State Chemistries for Fast Ion Conductors with Good Electrochemical Stability. *Angew. Chem., Int. Ed.* **2019**, *58*, 8039−8043.
(19) Liu, Y.; Wang, S.; Nolan, A. M.; Ling, C.; Mo, Y. Tailoring the Cation Lattice for Chloride Lithium-Ion Conductors. *Adv. Energy Mater.* **2020**, *10*, No. 2002356.
(20) Sebti, E.; Evans, H. A.; Chen, H.; Richardson, P. M.; White, K. M.; Giovine, R.; Koirala, K. P.; Xu, Y.; Gonzalez-Correa, E.; Wang, C.; Brown, C. M.; Cheetham, A. K.; Canepa, P.; Clement, R. J. Stacking Faults Assist Lithium-Ion Conduction in a Halide-Based Superionic Conductor. *J. Am. Chem. Soc.* **2022**, *144*, 5795−5811.
(21) Jordan, E.; Bell, R. G.; Wilmer, D.; Koller, H. Anion-promoted cation motion and conduction in zeolites. *J. Am. Chem. Soc.* **2006**, *128*, 558−567.
(22) Zhao, R.; Wu, Y.; Liang, Z.; Gao, L.; Xia, W.; Zhao, Y.; Zou, R. Metal−organic frameworks for solid-state electrolytes. *Energy Environ. Sci.* **2020**, *13*, 2386−2403.
(23) Xu, W.; Pei, X.; Diercks, C. S.; Lyu, H.; Ji, Z.; Yaghi, O. M. A Metal-Organic Framework of Organic Vertices and Polyoxometalate Linkers as a Solid-State Electrolyte. *J. Am. Chem. Soc.* **2019**, *141*, 17522−17526.
(24) Park, S. S.; Tulchinsky, Y.; Dinca, M. Single-Ion Li^+, Na^+, and Mg^{2+} Solid Electrolytes Supported by a Mesoporous Anionic Cu-Azolate Metal-Organic Framework. *J. Am. Chem. Soc.* **2017**, *139*, 13260−13263.
(25) Chi, X.; Li, M.; Di, J.; Bai, P.; Song, L.; Wang, X.; Li, F.; Liang, S.; Xu, J.; Yu, J. A highly stable and flexible zeolite electrolyte solid-state Li-air battery. *Nature* **2021**, *592*, 551−557.
(26) Lissner, F.; Krämer, K.; Schleid, T.; Meyer, G.; Hu, Z.; Kaindl, G. Die Chloride $Na_{3x}M_{2-x}Cl_6$ (M= La-Sm) und NaM_2Cl_6 (M = Nd, Sm): Derivate des UCl_3-Typs. Synthese, Kristallstruktur und Röntgenabsorptionsspektroskopie (XANES). *Z. Anorg. Allg. Chem.* **1994**, *620*, 444−450.
(27) Wickleder, M. S.; Meyer, G. Neue Derivate des UCl_3-Typs: Die Chloride und Bromide A (SrSm) Cl_6, A (SrEu) Cl_6 und A (BaLa) X_6 (A= Na, Ag; X= Cl, Br). *Z. Anorg. Allg. Chem.* **1998**, *624*, 1577−1582.
(28) Lee, W. K.; Liu, J. F.; Nowick, A. S. Limiting behavior of ac conductivity in ionically conducting crystals and glasses: A new universality. *Phys. Rev. Lett.* **1991**, *67*, 1559−1561.
(29) Dhahri, A.; Dhahri, E.; Hlil, E. K. Electrical conductivity and dielectric behaviour of nanocrystalline $La_{0.6}Gd_{0.1}Sr_{0.3}Mn_{0.75}Si_{0.25}O_3$. *RSC Adv.* **2018**, *8*, 9103−9111.
(30) Mauritz, K. A. Dielectric relaxation studies of ion motions in electrolyte-containing perfluorosulfonate ionomers. 4. Long-range ion transport. *Macromolecules* **1989**, *22*, 4483−4488.
(31) Holzwarth, U.; Gibson, N. The Scherrer equation versus the 'Debye-Scherrer equation'. *Nat. Nanotechnol.* **2011**, *6*, 534.
(32) Tatsumisago, M.; Yamashita, H.; Hayashi, A.; Morimoto, H.; Minami, T. Preparation and structure of amorphous solid electrolytes based on lithium sulfide. *J. Non-Cryst. Solids* **2000**, *274*, 30−38.
(33) Nakagawa, Y.; Kimura, T.; Ohki, T.; Isobe, S.; Shibayama, T. Effect of mechanical milling on lithium-ion conductivity of $LiAlH_4$. *Solid State Ionics* **2021**, *365*, No. 115656.
(34) Rao, R. P.; Sharma, N.; Peterson, V.; Adams, S. Formation and conductivity studies of lithium argyrodite solid electrolytes using in-situ neutron diffraction. *Solid State Ionics* **2013**, *230*, 72−76.
(35) Andersen, J. N.; Hennig, D.; Lundgren, E.; Methfessel, M.; Nyholm, R.; Scheffler, M. Surface core-level shifts of some 4d-metal single-crystal surfaces: Experiments and ab initio calculations. *Phys. Rev. B: Condens. Matter Mater. Phys.* **1994**, *50*, 17525−17533.
(36) Wertheim, G.; Buchanan, D.; Rowe, J.; Citrin, P. Surface-ion core-level shifts in alkali halides. *Surf. Sci.* **1994**, *319*, L41−L46.
(37) Wren, A. G.; Phillips, R. W.; Tolentino, L. U. Surface reactions of chlorine molecules and atoms with water and sulfuric acid at low temperatures. *J. Colloid Interface Sci.* **1979**, *70*, 544−557.
(38) Shadle, S. E. *Ligand K-edge x-ray absorption spectroscopic studies of the electronic structure of inorganic model complexes and metalloprotein active sites*; Stanford University, 1994.
(39) Soldatov, A.; Ivanchenko, T.; Della Longa, S.; Kotani, A.; Iwamoto, Y.; Bianconi, A. Crystal-structure effects in the Ce L_3-edge x-ray-absorption spectrum of CeO_2: Multiple-scattering resonances and many-body final states. *Phys. Rev. B: Condens. Matter Mater. Phys.* **1994**, *50*, 5074.
(40) Mehrer, H. *Diffusion in solids: fundamentals, methods, materials, diffusion-controlled processes*; Springer Science & Business Media, 2007; vol. *155*.
(41) Springer, T.; Lechner, R. *Diffusion in condensed matter*; Springer: New York, 2005.
(42) Yu, C.; Ganapathy, S.; Hageman, J.; Van Eijck, L.; Van Eck, E. R.; Zhang, L.; Schwietert, T.; Basak, S.; Kelder, E. M.; Wagemaker, M. Facile synthesis toward the optimal structure-conductivity characteristics of the argyrodite Li_6PS_5Cl solid-state electrolyte. *ACS Appl. Mater. Interfaces* **2018**, *10*, 33296−33306.
(43) Uitz, M.; Epp, V.; Bottke, P.; Wilkening, M. Ion dynamics in solid electrolytes for lithium batteries. *J. Electroceram.* **2017**, *38*, 142−156.
(44) Wilkening, M.; Heitjans, P. From Micro to Macro: Access to Long-Range Li^+ Diffusion Parameters in Solids via Microscopic $^{6,7}Li$ Spin-Alignment Echo NMR Spectroscopy. *ChemPhysChem* **2012**, *13*, 53−65.
(45) Yu, C.; Ganapathy, S.; van Eck, E. R.; van Eijck, L.; Basak, S.; Liu, Y.; Zhang, L.; Zandbergen, H. W.; Wagemaker, M. Revealing the relation between the structure, Li-ion conductivity and solid-state

https://doi.org/10.1021/jacs.2c09446
J. Am. Chem. Soc. 2023, 145, 2183−2194

battery performance of the argyrodite Li_6PS_5Br solid electrolyte. *J. Mater. Chem. A* **2017**, *5*, 21178−21188.
(46) Duchêne, L.; Lunghammer, S.; Burankova, T.; Liao, W.-C.; Embs, J. P.; Copéret, C.; Wilkening, H. M. R.; Remhof, A.; Hagemann, H.; Battaglia, C. Ionic conduction mechanism in the $Na_2(B_{12}H_{12})_{0.5}(B_{10}H_{10})_{0.5}$ closo-borate solid-state electrolyte: Interplay of disorder and ion−ion interactions. *Chem. Mater.* **2019**, *31*, 3449−3460.

https://doi.org/10.1021/jacs.2c09446
J. Am. Chem. Soc. 2023, 145, 2183−2194